JOURNAL OF ROCK MECHANICS

VOL. 9, NO. 4, PP. 1-17.

https://doi.org/10.22034/IRSRM.2026.468758.0141

Hybrid Numerical Modeling of Blast Response in Steel–Soil Layered Media

Mohammad Hossein Mokhtarzadeh[1]; Ehsan Taheri[1]*

1- Department of Rock Mechanics, Faculty of Mining and Materials Engineering, Tarbiat Modares University, Tehran, Iran.

Received: 18 January 2026 Accepted: 23 February 2026

(* Corresponding Author: e_taheri@modares.ac.ir)

Keywords

Discrete Element Method
Finite Element Method
Smoothed Particle Hydrodynamics
Explosion
Blasting Damage
Steel–soil layer

Abstract

Accurate prediction of blast-induced damage in layered geotechnical systems is essential for the resilient design of underground protective structures. However, the complex physics of explosion—involving extreme deformation, multi-material interaction, and high strain rates—poses significant challenges for both experimental replication and single-method numerical modeling. To address this gap, the present study develops a hybrid computational framework coupling Smoothed Particle Hydrodynamics (SPH), the Discrete Element Method (DEM), and the Finite Element Method (FEM) to simulate damage in a steel–soil layered configuration subjected to explosive loading. The proposed model assigns each constituent material its most suitable numerical approach: SPH handles the TNT explosive charge, capturing large deformation and fragmentation without mesh distortion; DEM models the granular soil layer, accounting for particle-scale interactions and contact failure; FEM discretizes the steel sheet, enabling precise stress–strain evaluation. The Johnson–Cook constitutive model is employed as the damage criterion for the steel layer, incorporating strain hardening, strain rate sensitivity, and thermal softening effects. For the soil, contact failure is defined to govern particle debonding and detachment. The thermodynamic behavior of the detonation products is described by the Jones–Wilkins–Lee (JWL) equation of state. The paper details the fundamental principles, coupling algorithms, and interface conditions among the three methods. Simulation results demonstrate that the integrated SPH-DEM-FEM approach effectively reproduces key damage patterns, including steel perforation, soil cratering, and layer delamination. This validated multi-physics model provides researchers with a powerful numerical tool to explore various blast scenarios, charge geometries, and layer properties, thereby advancing the understanding of explosion–structure interaction in layered media.

I. INTRODUCTION

In the design of subterranean structures, it is imperative to assess the response of the support system to dynamic loading. The stability of such structures hinges not only on the type of support system employed, but also on its capacity to withstand dynamic loads such as seismic conditions, impacts, and explosions. Various support systems, including steel frames, concrete lining, wooden support systems, and rock bolts, can be employed to bolster subterranean structures. A comprehensive analysis of how each support system responds to dynamic loading is indispensable in ascertaining its appropriateness for a particular project. By comprehensively evaluating the performance of diverse support systems under dynamic loads, engineers can make judicious decisions about the most suitable system for a given project, thus guaranteeing the stability and safety of the subterranean structure. In summary, the scrutiny of the support system's response to dynamic loading is integral in safeguarding subterranean structures against dynamic loads. The outcomes of such analyses wield substantial influence in the configuration and selection of apt support systems, profoundly augmenting the safety and dependability of subterranean structures [1–3]. In a scholarly investigation by Thai et al. [4], the phenomenon of local damage to reinforced concrete tunnels resulting from ballistic missile assaults was subjected to examination through finite element analysis. Explosions constitute a form of dynamic loading, characterized as a random or spontaneous event. For instance, the detonation of a car transporting flammable substances, such as gasoline or gas, within a tunnel, results in an internal explosion that can lead to tunnel collapse, thereby obstructing communication pathways between two areas. Surface explosions, stemming from construction activities or spontaneous events, may also occur; these can have profound consequences, particularly when situated beneath a tunnel. Fundamental to the stability of subterranean structures are two primary explosion factors: ground

vibration and the propagation of the blast wave, alongside the pressure exerted by gases expanding as a result of explosive combustion. These elements play an indispensable role in determining the structural integrity of subterranean constructions [4,5]. Recently, several advanced numerical methods have been developed to simulate such dynamic events. For instance, Yosef et al. [6] investigated large deformation pile-soil interaction under lateral vehicle impact using hybrid SPH+FEM and EFG+FEM models, demonstrating the capability of coupled methods in geotechnical impact problems. Similarly, Chen and Zu [7] performed theoretical and experimental studies on the performance of multi-layer composite targets against shaped charge jets, highlighting the importance of layered protective systems. conducted a three-dimensional simulation analysis of the impact of excavation on non-level crossing tunnels, which underscores the critical need for robust numerical tools in underground construction and safety assessments• Underground structures are not as safe as surface structures from escaping smoke and gases from explosions and are more difficult to control. A dangerous circumstance, such as an explosion, is essential for underground structures for five reasons [3,5–10]:

• Underground structures bear a default slag weight, and any damage to their maintenance systems causes disturbances in stress balancing and the destructive effect of other loads on the structure.

• Cracks and water leakage into the tunnel may occur due to the explosion, leading to extended damage over time.

• The construction of an underground structure is based on geological surveys, and an explosion can cause significant financial losses and time to rebuild.

• Repetition of surface or internal explosions inside Several numerical studies have been conducted by different researchers, for example [3,11], investigation of the explosion inside the underground structure by the finite element method can be mentioned, by the discrete element method like [12,13] and by the SPH method [14,15]. A coupled method numerical modeling is done like (DEM FEM) [16–18], and (SPH-FEM) like [19–21]. Beyond these, recent advancements have shown the effectiveness of fully integrated multi-method approaches. For example, Zhou et al. [22] used an integrated SPH-DEM-FEM model with a cohesive element method to analyze the breakage mechanism of bedded sandstone under abrasive water jet impact, demonstrating the power of such coupling in capturing complex failure modes. Huang, Zhu, and Chen [23] also developed a coupled peridynamics–SPH model specifically for simulating buried explosion-induced soil fragmentation and cratering, which is highly relevant to the physics of the current study.

Beyond blast-specific applications, similar coupled and analytical methods have been successfully employed in other geomechanics contexts. For instance, Sharafisafa and Aliabadian [24] investigated the effect of Discrete Fracture Network (DFN) density on hydraulic fracturing using numerical simulations, highlighting the importance of fracture distribution in rock mass behavior. Sarfaraz and Khosravi [25] proposed an analytical method based on stress arching theory for the stabilization of soil slopes using a single row of piles, offering a simplified yet robust tool for geotechnical design. These studies, although focused on different loading scenarios, demonstrate the broader utility of advanced numerical and analytical approaches in addressing complex soil and rock mechanics problems.

In this article, we have explored a unified method for numerical modeling. This method assumes the soil and steel as a layered structure and utilizes the SPH method to simulate an explosion. We then proceed to investigate each of these methods.

The specific configuration studied herein—a steel plate embedded in a soil layer subjected to an underground explosion—has direct practical relevance. Such layered protective systems are commonly used in: (i) buried ammunition storage facilities to prevent sympathetic detonation; (ii) reinforced tunnel linings in strategic transportation corridors; (iii) blast barriers for underground pipelines and utility corridors; and (iv) protective structures for subway systems in high-risk zones. Understanding the damage mechanisms (perforation, cratering, delamination) is critical for the design and retrofitting of these infrastructure assets.

The novelty of the present work lies not in the individual numerical methods (SPH, DEM, FEM are well-established), but in their integrated application to the specific problem of steel-soil layered media under blast loading. Existing studies typically use either SPH-FEM for explosion-structure interaction or FEM-DEM for granular media, but rarely all three simultaneously. For instance, while several studies have successfully applied SPH-DEM-FEM coupling to other fields, such as debris-flow barrier performance evaluation by Wang et al. and bed scour erosion analysis in debris-flow channels by Wang et al. [39], their application to underground blast scenarios with steel-soil layered systems remains limited. Commercial coupling approaches (e.g., Abaqus CEL) treat soil as a continuum and cannot capture particle ejection, while pure DEM simulations lack a realistic explosion model. Our framework addresses these gaps by: (i) using SPH for the explosive charge to avoid mesh distortion, (ii) employing DEM for sand to simulate cratering and particle ejection, and (iii) retaining FEM for the steel plate to evaluate stress and perforation. The key new insight is that the simultaneous coupling of all three methods is computationally feasible and provides a more complete picture of blast damage than any single-method or two-method approach.

II. METHODOLOGY

In this article modeling methodology encompasses three interconnected numerical techniques (SPH-FEM-DEM). It employs the Discrete Element Method (DEM) for soil modeling, the Finite Element Method (FEM) for steel layer modeling, and the Smoothed Particle Hydrodynamics (SPH) method for modeling the explosive substance (TNT). The explanation of the DEM and the SPH method is concise, practical, and easily comprehensible.

A. Discrete element method

The Discrete Element Method (DEM) plays a crucial role in modeling solids. This method can accurately model solids, including dispersions, detachments, and fractures. In the DEM, particles can be connected through sets of springs if they are in each other's domain. Specifically, in linear spring models, springs only act when particles overlap; no force is produced otherwise. On the other hand, bonding models focus on the attachment and fracture of materials, considering the gap between particles for tensile force calculations. When dealing with problems unrelated to bonded particles, it is recommended to use the Hertz-Mindlin model instead of the linear spring model [26–28]. The majority of Discrete Element Method (DEM) bonding techniques are founded on the principles of contact and parallel bonding. The parallel bonding model can be integrated with either the linear spring model or the contact bonding model [29]. However, the former is the more prevalent choice and is the approach being utilized in this context. The total force applied to each particle in the DEM is:

$$F^{total} = \sum F^{CF} + F^{b} + F^{d} + \sum F^{ext} \quad (1)$$

where F^{total} is the total force, $\sum F^{CF}$ is the contact force, F^{b} is the body force, F^{d} is the damping force and $\sum F^{ext}$ is the sum of external forces. In the Discrete Element Method (DEM), both external and contact forces result in alterations to the linear and angular momentum of the DEM particles. This section will elaborate on how the contact, momentum, and damping forces are computed, as well as the foundation for the parallel bond [28,29].

1) The linear spring models

The linear spring model includes two types of springs; one lies on the contact plane and another one is in the direction of normal to the contact plane. Therefore, the equations to calculate normal n_i and shear t_i vectors of each contact plane are [28]:

$$n_i = \frac{x_i^{[B]} - x_i^{[A]}}{d} \quad (2)$$

$$t_i = (-n_2, n_1) \quad (3)$$

Where superscripts B and A denote the circular particles that are in contact, x_i is the reference coordinates, and d is the distance which can simply be calculated as:

$$d = \left|x_i^{[B]} - x_i^{[A]}\right| = \sqrt{\left(x_i^{[B]} - x_i^{[A]}\right)\left(x_i^{[B]} - x_i^{[A]}\right)} \quad (4)$$

The size of the overlap between the two particles is:

$$U^n = d - R^{[A]} - R^{[B]} \quad (5)$$

The normal spring model is only valid until U^n is negative. The Discrete Element Method (DEM) involves particles that are slightly overlapped in order to form bonds between them. If we calculate the overlap between particles directly using equation 5 to compute the DEM forces, the initial forces in the simulation would be non-zero. Therefore, utilizing the direct approach to determine overlaps is impractical. Consequently, it is better to calculate the overlap incrementally using relative velocity:

$$\Delta U^n = \left(x_i^{[B]} - x_i^{[A]}\right) n_i \Delta t \quad (6)$$

In this equation, ΔU^n is the incremental overlap, Δt is the elapsed time of each calculation cycle and x_i is the velocity.

Note that, the value of shear displacement cannot be captured directly like equation 5 for the normal overlap, and can only be achieved incrementally using the following:

$$\Delta U^s = V^s \Delta t \quad (7)$$

Where V^s is the relative shear velocity and is computed by:

$$V^s = \left(x_i^{[B]} - x_i^{[A]}\right) t_i - \omega_3^{[B]} \left(R^B + \frac{U^n}{2}\right) - \omega_3^{[A]} \left(R^A + \frac{U^n}{2}\right) \quad (8)$$

Where ω_3 denotes the rotational velocity in the z-direction. After the calculation of relative normal and shear displacements at the contact point, the contact forces can be updated using the normal and shear spring constants (k^n, k^s) using the following equations [28]:

$$\Delta F^n = k^n \Delta U^n \quad (9)$$

$$\Delta F^s = k^s \Delta U^s \quad (10)$$

$$F^n \leftarrow F^n + \Delta F^n \quad (11)$$

$$F^s \leftarrow F^s - \Delta F^s \quad (12)$$

$$F^s = \min(F^s, \mu F^n) \quad (13)$$

$$F_i^{LSMCF[A,B]} = F^s t_i - F^n n_i \quad (14)$$

$$M_3^{[A]} \leftarrow M_3^{[A]} - F^s \left(R^{[A]} + \frac{U^n}{2}\right) \quad (15)$$

where $\leftarrow$ denotes the assignment of its right-hand side value to its left-hand side variable, F^n is the normal force, F^s is the shear force, $F_i^{LSMCF[A,B]}$ is the linear spring model's force in the direction from particle A to particle B, and μ is the friction coefficient. It is also worth pointing out that equation 13 is used to enforce the slip condition [28]. Only shear force is responsible for producing angular momentum; Therefore, the moment caused by this contact force is:

$$M_3^{[A]} \leftarrow M_3^{[A]} - F^s \left(R^{[A]} + \frac{U^n}{2}\right) \quad (16)$$

Where $M_3^{[A]}$ is the total moment of particle A. One should bear in mind that in equation 16, the moment

vector is reduced to M_3 since here two-dimensional analyses are carried out.

2) Parallel Bond

In this perception of the bonded particles, each pair is connected to a beam-like element with the cross-section area of A and moment of inertia of I, called cement. On this account, the cement elements are capable of transmitting and tolerating both axial forces and moments until a maximum value is reached. The model is defined by five bonding parameters: the normal stiffness $\overline{k}^n$, the shear stiffness $\overline{k}^s$,the normal strength $\overline{\sigma}_c$, the shear strength $\overline{\tau}_c$ and the bond radius $\overline{R}$. The bond radius is the radius of the cement and is equal to the mean or equivalent radius of two bonded particles multiplied by a constant$\left(\bar{R} = \alpha\frac{R^{[A]}+R^{[B]}}{2}\ or\ \bar{R} = \alpha\frac{R^{[A]}R^{[B]}}{R^{[A]}+R^{[B]}}\right)$. The forces F and M caused by the presence of a parallel bond are expressed incrementally by:

$$F = \overline{F_s}t - \overline{F_n}n \quad (17)$$

$$M = \overline{M_3} \leftarrow \overline{M_3} - \overline{k_n}I\Delta\theta_3 \quad (18)$$

Where $\Delta\theta_3$ is the increment of rotation around the third axis $\left(\Delta\theta_3 = \left(\omega_3^{[B]} - \omega_3^{[A]}\right)\Delta t\right)$.$\overline{F}^n$ And $\overline{F}^s$ are computed through:

$$\overline{F_n} \leftarrow \overline{F_n} + \overline{k_n}A\Delta U^n \quad (19)$$

$$\overline{F_s} \leftarrow \overline{F_s} - \overline{k_s}A\Delta U^s \quad (20)$$

Now that the parallel bond's momentum and forces are calculated, they must be evaluated against the bond's normal and shear strength. These criteria are expressed by:

$$\frac{\overline{F_n}}{A} + \frac{|\overline{M_3}|\bar{R}}{I} \geq \overline{\sigma_c} \quad (21)$$

$$\frac{|\overline{F_s}|}{A} \geq \overline{\tau_c} \quad (22)$$

While these criteria are met, the bond between each bonded particle remains intact but as soon as violated the bond would disappear and the contact behavior would only be that of the linear spring model. Subsequently, if the bond is not broken, the forces and moments are added to the corresponding total values:

$$F_i^{CF[A]} \leftarrow F_i^{CF[A]} - \overline{F_i} \quad (23)$$

$$M_3^{[A]} \leftarrow M_3^{[A]} - \overline{F_s}\left(R^{[A]} + \frac{U^n}{2}\right) - \overline{M_3} \quad (24)$$

3) Damping

When utilizing the Discrete Element Method (DEM), it is essential to consider the predominance of elasticity in interactions unless damping is deliberately applied. Damping plays a crucial role in reducing energy loss by mitigating unbalanced forces, thus promoting stability in the later stages of DEM simulations. Without damping, achieving stability becomes unattainable and may yield unreliable conclusions. Various methods can be employed to introduce damping into a system, such as mass, viscous, and local damping. The mass damping method, while once utilized, is no longer favored due to its tendency to introduce additional body forces, dependence on the stiffness matrix parameter, and uniform damping effect on all particles. Viscous damping is suitable for simulations involving free fall or particle impact; however, it cannot efficiently guide a simulation to its final steady state and is ineffective in influencing the cement part of the parallel bond. Moreover, the impact of viscous damping on the linear spring model overlooks the substantial magnitude of parallel bond springs, making its effect negligible in their presence. As a result, local damping serves as the preferred method, albeit less suitable for impact-related problems, but showing promise when appropriately applied. The calculation of local damping for each particle is necessitated within this approach [28,30]:

$$F_i^d = -\alpha\left|F_i^U\right|sign(v_i) \quad (25)$$

where α is the local damping constant, F_i^U is the unbalanced force and $sign()$ is a function that returns the signature of an input variable (positive = +1, zero = 0, negative = -1). Regularly, the constant is taken to be 0.7, yet in dynamic solutions, 0.157 is used, which corresponds to 5 percent of critical damping of a structure.

B. Smoothed Particle Hydrodynamics

The Smoothed Particle Hydrodynamics (SPH) method, although applicable to simulating all phases, is commonly utilized to replicate fluid dynamics. This study also employs SPH to model water behavior. In SPH, each point represents the properties of its surroundings. As the distance to the center of a point within its domain decreases, the influence of its surrounding properties increases. With the position vector of an arbitrary point within its domain, the general formulation of SPH is derived from the following equation [31]:

$$f(x) = \int_\Omega f(x)\delta(x-x)d\,\Omega \quad (26)$$

Where δ denotes the Dirac delta function, x is the position vector of every point in the domain of x and f is the property function. Having δ replaced by a smoothing function (W) and discretizing Ω, the basic form of the SPH is:

$$f\left(x^{[A]}\right) = \sum_{B=1}^{n} f\left(x^{[B]}\right)W\left(x^{[A]} - x^{[B]}, h\right)\frac{m^{[B]}}{\rho^{[B]}} \quad (27)$$

Where n is the total number of points in the domain, h is the smoothing length, m is the mass, and ρ is the density. In various research, usually, Spline and Wendland smoothing functions (kernels) are used. Here based on the recommendation [28,32], Wendland kernel is employed which has the following formulation (for two-dimensional):

$$W(q) = \begin{cases} \frac{7}{4\pi h^2}(1-\frac{q}{2})^4(2q+1) & 0 < q < 2 \\ 0 & 2 < q \end{cases} \quad (28)$$

Where q is dh in which d is the distance. On many occasions, an approximation of divergence (for vector functions) and gradient (for scalar functions) of a certain property function is needed, which were derived from different perspectives based on the need and knowledge of SPH developers [28,34]. Here, to

apply divergence and gradient, the following equations are used, respectively.

$$\nabla \cdot f\left(x^{[A]}\right) = -\sum_{B=1}^{n} \frac{m^{[B]}}{\rho^{[B]}}\left(f\left(x^{[A]}\right) - f\left(x^{[B]}\right)\right) \cdot \nabla W\left(x^{[A]} - x^{[B]}, h\right) \quad (29)$$

$$\nabla f(x^{[A]}) = -\rho^{[A]} \sum_{B=1}^{n} m^{[B]} \left(\frac{f(x^{[A]})}{\left(\rho^{[A]}\right)^2} + \frac{f(x^{[B]})}{\left(\rho^{[B]}\right)^2}\right). \nabla W(x^{[A]} - x^{[B]}, h) \quad (30)$$

It is worth mentioning that equation 30 is also used for taking the divergence of a tensor. The fundamental governing equations of fluid dynamics are the conservation of mass, momentum, and energy. These are the three basic physical laws of conservation. Generally, the third law is used when the change in energy is of high importance to a simulation's result, so it is omitted here.

1) Continuity Equation

According to the conservation of mass, the continuity equation is derived:

$$\frac{\partial \rho}{\partial t} = -\rho \nabla \cdot v \quad (31)$$

Where ρ is the density, $\frac{D}{D_t}$ is the material time derivative, $\nabla.$ is the divergence, and v is the velocity. The continuity equation states that the rate of the mass imported to the system minus the rate of the mass exported from it, is equal to the accumulation of mass in that system.

One of the key considerations in Smoothed Particle Hydrodynamics (SPH) is the approximation of a fundamental property, denoted as this property plays a pivotal role in the formulation of nearly all SPH equations. Any misestimation of could lead to significant inaccuracies in the calculations of other approximations. Given the uneven distribution of densities in multiphase simulations, it becomes essential to employ an approximation, such as the following equation, which offers the advantage of utilizing volume rather than density [35,36].

$$\frac{D\rho^{[A]}}{Dt} \simeq \rho^{[A]} \sum_{B=1}^{n} \frac{m^{[B]}}{\rho^{[B]}}\left(v^{[A]} - v^{[B]}\right) \cdot \nabla W\left(x^{[A]} - x^{[B]}, h\right) \quad (32)$$

This equation is derived from substituting 29 in 31.

2) Momentum Equation

The equation of momentum is derived based on the equivalency of forces acting on an infinitesimal box in every local axial direction. This equation is expressed as:

$$\frac{Dv_i}{Dt} = -\frac{1}{\rho}\frac{\partial p}{\partial x_i} + \frac{1}{\rho}\frac{\partial \tau_{ij}}{\partial x_i} + F_i \quad (33)$$

Where p is the pressure,τ_{ij} is the viscosity stress tensor, and F_i is the body force per mass. This equation consists of three terms, the gradient of pressure, divergence of viscosity stress tensor, and body force. The interpretation of the first term by the SPH is:

$$\left(-\frac{1}{\rho}\frac{\partial p}{\partial x_i}\right)^{[A]} = \sum_{B=1}^{n} m^{[B]} \left(\frac{p^{[A]}}{\left(\rho^{[A]}\right)^2} + \frac{p^{[B]}}{\left(\rho^{[B]}\right)^2}\right) \nabla W\left(x^{[A]} - x^{[B]}, h\right) \quad (34)$$

This is achieved by substituting equation 30 in the pressure gradient term of equation 33. As there is no way of knowing the pressure based on the continuity and momentum equations, a concept known as "artificial compressibility" is used, inspired by the existence of the well-known direct correlation between density and pressure in fluids. One of the equations, founded on this concept is the "Tait equation":

$$\rho = \frac{100\rho_0 v_{max}^2}{\gamma}\left(\left(\frac{\rho}{\rho_0}\right)^{\gamma} - 1\right) \quad (35)$$

Where ρ_0 is the reference density, v_{max} is the maximum possible velocity in an environment, and γ is a constant usually taken to be seven [32-34].

For computing the divergence of the viscosity tensor, generally, two approaches exist [31]:

One) At first strain is calculated for each point, then, knowing that $\boldsymbol{\tau} = \mu\boldsymbol{\epsilon}$ (where μ is the dynamic viscosity and ϵ is the strain and substituting equation 30, the divergence of $\boldsymbol{\tau}$ is figured out.

Two) using a concept called artificial viscosity. Artificial viscosity used to be utilized only for inviscid dissipations (damping) in simulations, especially suitable for shock problems. Later this concept was further developed to involve viscous dissipation even for low Reynolds numbers [31]. In this paper, the second approach was preferred considering its relatively higher run-time speed, and the below equation is used.

$$\left(\frac{1}{\rho}\frac{\partial \tau_{ij}}{\partial x_i}\right)^{[A]} = \sum_{B=1}^{n} m^{[B]}\left(\mu^{[A]} + \mu^{[B]}\right)\left(v^{[A]} - v^{[B]}\right)\frac{\left(x^{[A]} - x^{[B]}\right)\cdot\nabla W}{\rho^{[A]}\rho^{[B]}\left(\left|x^{[A]} - x^{[B]}\right|^2 + 0.01h^2\right)} \quad (36)$$

The term $0.01h^2$ in equation 36 is only added to avoid singularity. Finally, the body force term, for common simulations, is equal to the standard gravity.

3) Corrections

In employing a numerical method involving probabilities and uncertainties, it is imperative to implement corrective measures to address unnatural outcomes. Given that the kernels are contingent upon distance and smoothing length, the careful selection of the latter is crucial. It is suggested that the smoothing length be chosen in a manner that allocates 20 other points within its influential domain for a two-dimensional analysis [37]. An astute approach enables the smoothing length to dynamically adjust during a simulation, based on the fluctuation of density over an elapsed time step.:

$$\frac{Dh}{Dt} = -\frac{1}{n_d}\frac{h}{\rho}\frac{D\rho}{Dt} \quad (37)$$

Where nd denotes the dimension number. When the density of a point rises, its smoothing length and influential domain decrease. Using equation 37 begs for special care; since each point has its variable smoothing length, using the Kernel function for an interaction — twice — with two different smoothing lengths would violate the conservation rules. To clarify, in an extreme case, a point with a big h, acknowledges the presence of a point with a small h in its domain and involves it in its calculation but not

reciprocally. To resolve this issue a mean smoothing length must be considered $\left(h = \frac{h^{[A]}+h^{[B]}}{2}\right)$

Another problem in the SPH simulations is that wherever the pressure is negative, the probability of points clumping together is strong. One way to avoid it is by introducing an additional force term to Equation 34 [31]:

$$\left(-\frac{1}{\rho}\frac{\partial p}{\partial x_i}\right)^{[A]} \leftarrow \left(-\frac{1}{\rho}\frac{\partial p}{\partial x_i}\right)^{[A]} + \sum_{B=1}^{n}\frac{m^{[B]}}{100}\left(\frac{p^{[A]}}{\rho^{[A]}} + \frac{p^{[B]}}{\rho^{[B]}}\right)\left(\frac{W}{W(\Delta P,h)}\right)^4 \nabla W \quad (38)$$

Where ΔP is the points' initial spacing. Intending to diminish incoordination in movements of SPH points and bring some uniformity into the shape of fluids, a term called the XSPH correction is added to time integration methods [22,31,32]. This term is:

$$\frac{d\sigma^{[A]}}{dt} = \nu^{[A]} - \epsilon\sum_{B=1}^{n}\frac{m^{[B]}}{\rho^{[A,B]}}\left(\nu^{[A]} - \nu^{[B]}\right) \cdot \nabla W\left(x^{[A]} - x^{[B]}, h\right) \quad (39)$$

Where is the mean density value of points A and B, and ϵ is a number between 0 and 1, selected with a simulation's conditions. Throughout the literature of the SPH there are many other corrections for different simulation problems, based on the results; the corrections explained in this section, seem to suffice here.

4) Boundary Condition

Proper treatment of boundary conditions is essential for accurate SPH simulations. In the SPH method, the kernel function approximation (Equations 29 and 30) is valid when the kernel support domain is fully populated with neighboring particles. However, when particles approach a domain boundary, part of the kernel support domain lies outside the computational domain, leading to kernel truncation. This truncation introduces errors because the summation of kernel weights is no longer unity, and the approximation of gradients becomes inaccurate.

Several approaches exist to handle SPH boundary conditions. The first approach is to modify the kernel function or the approximation formulas near the boundary by reintroducing the omitted terms. The second, and more widely used, approach is to populate the boundary region with special particles that enforce the desired conditions. This second approach is adopted in the present study.

In this research, a fixed ghost particle method is employed for boundary conditions, following the approach of Adami et al. [36]. Stationary ghost particles are arranged in two or three layers along the lateral and bottom boundaries of the computational domain. These ghost particles share the same smoothing length and kernel function as the fluid (TNT) and soil particles. They do not move and are assigned physical properties (density, pressure, velocity) that enforce either no-slip or free-slip conditions as needed. At the lateral and bottom boundaries, a no-slip condition is applied: ghost particles carry zero velocity and their pressure is extrapolated from the nearest fluid particles, ensuring that fluid particles cannot cross the boundary and that the velocity gradient normal to the wall is zero.

At the top surface (ground surface), a free-surface boundary condition is naturally satisfied by the SPH method because no particles exist above this surface; no special treatment or ghost particles are required. This allows soil and explosion products to be ejected upward, realistically simulating crater formation and particle ejection.

For the DEM domain (soil particles), the same physical boundaries are modeled as rigid walls with a friction coefficient of 0.5 and a restitution coefficient of 0.5. This ensures consistency between the SPH and DEM boundary treatments.

The combination of fixed ghost particles for SPH and rigid walls for DEM provides stable and accurate boundary conditions throughout the simulation duration. No particle leakage or non-physical accumulation was observed at the boundaries.

III. NUMERICAL MODELING

The coupled numerical simulations are performed usi ng the commercial explicit finite element software LS -DYNA R11 (LSTC, Livermore, CA). This software p rovides a multi-physics framework that simultaneousl y solves FEM, SPH, and DEM within a single simulat ion using explicit time integration. The complete mod el consists of three distinct material domains: the expl osive charge (TNT), the steel plate, and the surroundi ng sand soil layer. Figure 1 presents a schematic cross -section of the model geometry.

Geometry and boundary conditions:

The soil layer (sand) has dimensions of 4 m in width a nd 2 m in depth. The steel plate is embedded horizont ally at a depth of 0.5 m from the ground surface, with a thickness of either 20 cm or 40 cm (two cases are ex amined). The TNT explosive charge is modeled as a s phere of radius 0.64 m (equivalent to 1814 kg TNT, c orresponding to a small delivery truck) and is position ed at a depth of 1.2 m from the ground surface, at a ho rizontal offset of 0.8 m from the left edge of the steel plate. The coordinate origin is defined at the ground s urface directly above the left edge of the plate. Non-re flecting boundary conditions are applied to the lateral and bottom boundaries of the soil domain to prevent w ave reflection, while the top surface is a free boundary . For SPH particles, a wall boundary condition is enfo

rced at the soil domain boundaries using fixed ghost p articles.

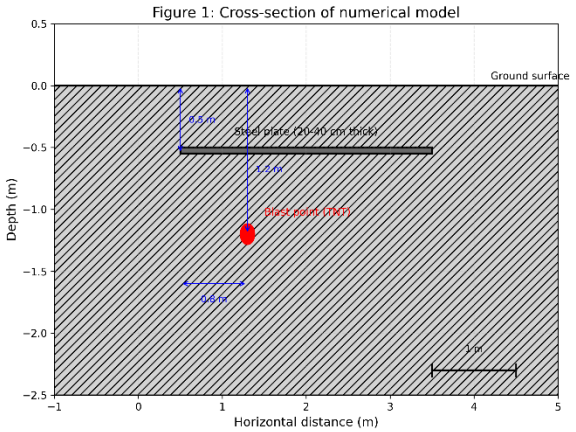

Figure 1-Schematic cross-section of the numerical model (not to scale; a scale bar of 1 m is provided at the bottom left corner). The steel plate (thickness 20 cm or 40 cm, width 4 m) is embedded horizontally at a depth of 0.5 m from the ground surface. The blast point (center of TNT charge, radius 0.64 m) is located at a depth of 1.2 m and at a horizontal distance of 0.8 m from the left edge of the steel plate. The coordinate origin is at the ground surface directly above the left edge of the plate. All dimensions are in meters.

A. TNT (SPH model)

The explosion of a small delivery truck under the steel plate is simulated. According to Table 1, the TNT equivalent charge for this vehicle (small delivery truck) is estimated as 1814 kg [8]. In this article, TNT is simulated as a sphere. With a mass density of 1630 kg/m³ (see Table 2), the volume of the TNT charge is 1.113 m³, which yields a radius of approximately 0.64 m.

The explosive charge is modeled using the Smoothed Particle Hydrodynamics (SPH) method. The TNT sphere is discretized with approximately 8,234 SPH particles with an initial particle spacing of 1.2 cm, which provides sufficient resolution to capture the detonation wave propagation and pressure distribution. The Jones–Wilkins–Lee (JWL) equation of state is employed to describe the pressure generated by the detonation products. The JWL equation is written as Equation (40):

$$P = A\left(1 - \omega/(R_1 V)\right)e^{-R_1 V} + B\left(1 - \omega/(R_2 V)\right)e^{-R_2 V} + (\omega E)/V \quad (40)$$

where:

- P is the pressure caused by the explosion,
- V is the relative volume of the detonation products,
- E is the internal energy per unit volume of the explosive,
- A, B, R1, R2, ω are material constants (explosive constants) [3,37].

This equation of state can obtain the pressure from the explosion by accounting for the chemical reaction of the TNT [39]. The TNT properties and JWL parameters used in this study are listed in Table 2 [6]. No delay time is considered in the modeling; detonation is initiated at the center of the sphere at time t = 0. The spherical TNT charge within the soil layer is shown in Figure 1.

Table 1-TNT equivalent filling a vehicle [3]

Vehicle Description	TNT equivalent (Kg.)
Sedan	227
SUV or Van	454
Small Delivery Truck	1814
Container or Water Truck	4536
Semi-Trailer	27216

Table 2-TNT properties and JWL parameters for TNT [3]

Parameter	Measure
Mass density (kg/m3)	1630
A (MPa)	373800
B (MPa)	374700
Ω	0.35
R1	4015
R2	0.9
Detonation energy density (kJ/kg)	3680
Detonation wave speed (m/s)	6930

B. Steel plate (FEM model)

The steel plate is simulated using the Finite Element M ethod (FEM). Two different thicknesses are considere d in this study: 20 cm and 40 cm, to investigate the eff ect of plate thickness on blast resistance. The plate wi dth is 4 m, matching the soil domain width. The mesh size is selected based on a convergence study (present ed in Section IV-B), which determined an optimal ele

ment size of 5 mm through the thickness and 10 mm a long the plate length. Eight-node hexahedral solid ele ments with reduced integration are used.

The damage criterion for the steel plate is governed b y the Johnson–Cook (J-C) constitutive model. The Joh nson–Cook model can describe the relationship betwe en stress (σ) and strain (ε) of metallic structures under conditions of large deformation, high strain rate, and e levated temperatures (T*). The Johnson–Cook flow st ress equation is written as:

$$\sigma = (A + B\varepsilon^{N})(1 + Cln\dot{\varepsilon}^{*})(1 - T^{*m}) \quad (41)$$

where:

- σ is the equivalent flow stress,
- ε is the equivalent plastic strain,
- ε̇* = ε̇ / ε̇_0 is the dimensionless plastic strain rate (ε̇_0 = 1 s⁻¹),
- T* = (T - T_room) / (T_melt - T_room) is the homologous temperature,
- A is the yield stress at reference strain rate,
- B is the strain hardening coefficient,
- N is the strain hardening exponent,
- C is the strain rate sensitivity coefficient,
- m is the thermal softening exponent.

It should be noted that temperature effects are neglected in this study. The adiabatic assumption is justified because the time scale of blast loading (several milliseconds) is too short for significant heat conduction to occur, and the primary damage mechanisms under consideration (perforation, cracking, and cratering) are mechanically driven. Therefore, the thermal softening term (1 - T^{*m}) is set to unity. The strain rate sensitivity term (1 + C ln ε*) is retained because blast loading involves extremely high strain rates. The Johnson–Cook damage (fracture) criterion is also employed, with element deletion when the damage parameter reaches unity. The J-C parameters used in this study are listed in Table 3 for AISI-1045 steel [40]. The discretized steel plate within the model geometry is shown in Figure 1.

Table 3-Johnson-Cook parameters for AISI-1045 steel [34]

A (MPa)	B (MPa)	C	N	m	D1	D2	D3	D4	D5
50.103	176.091	0.095	0.5176	0.6622	0.05	3.44	-2.12	0.002	0.61

D1 to D5 are Johnson-Cook damage (fracture) parameters for AISI-1045 steel, obtained from [40].

C. Soil (DEM model)

The soil studied in this research is dry sand. It is mode led using the Discrete Element Method (DEM). The s and particles are represented as spheres with radii unif ormly distributed between 2 mm and 5 mm. The total number of particles generated within the soil domain (4 m width × 2 m depth) is approximately 45,000, whi ch provides a representative volume element while ma intaining computational efficiency. The particle size d istribution has been selected optimally to avoid excess ive computational cost while capturing the macroscop ic behavior of the sand.

The contact behavior between soil particles, as well as between soil particles and the steel plate (or boundarie s), is governed by the Hertz–Mindlin contact model. T his model accounts for the normal and tangential elast ic interactions, damping, and friction. The normal forc e is calculated based on the overlap distance and the e quivalent Young's modulus, while the tangential force follows the Mindlin-Deresiewicz theory with a frictio n limit defined by Coulomb's law. No parallel bondin g is used because the sand is cohesionless; therefore, p articles do not experience tensile forces and detach fre ely when the contact force becomes tensile or when th e shear stress exceeds the friction limit.

The contact between the soil layer and the steel plate i s modeled using the same contact algorithm described in Section D (Coupling conditions at interfaces). Spec ifically, the DEM particles interact with the FEM elem ents of the steel plate via a penalty-based node-to-surf ace contact. A friction coefficient of 0.4 is defined for the soil–steel interface.

The mechanical properties of the soil particles are as f ollows:

- Poisson's ratio: ν = 0.2
- Shear modulus between particles: G = 29 GPa
- Specific weight (mass density) of soil: ρ = 1920 kg/ m³
- Internal friction coefficient of particles: μ = tan(40°) ≈ 0.84 (corresponding to a friction angle of 40 degree s)
- Restitution coefficient (for normal impacts): e = 0.5

To account for the high strain rates induced by blast lo ading, a strain-rate dependent Mohr-Coulomb model i s employed. The dynamic friction angle φ_dyn is calc ulated as $\varphi_{dyn} = \varphi_{static} \cdot (1 + \beta \log_{10}(\dot{\varepsilon}/\dot{\varepsilon}_0))$, where β = 0.05 is the rate sensitivity parameter, ε̇ is the curre nt strain rate, and ε̇₀ = 1 s⁻¹ is the reference strain rate [42]. This formulation captures the increase in soil str ength under rapid loading.

The walls (boundaries of the soil domain) are conside red rigid with a friction coefficient of 0.5 and a restitu tion coefficient of 0.5. These walls are fixed and do n ot deform. No-slip condition is enforced at the lateral and bottom boundaries, while the top surface is free. T he spatial relationship between the soil particle assem bly, the steel plate, and the TNT charge is shown in Fi gure 1.

D. Coupling conditions at interfaces

The coupling between the three numerical methods is handled by LS-DYNA's built-in multi-physics contact algorithms:

- FEM–DEM coupling: The contact between the steel plate (FEM elements) and the soil particles (DEM) is defined using the CONTACT_NODES_TO_SURFACE keyword. A penalty-based algorithm computes normal and tangential forces with a friction coefficient of 0.4. The steel surface is treated as a rigid master surface relative to the deformable DEM particles.
- SPH–FEM coupling: The TNT SPH particles interact with the steel plate through the CONTACT_AUTOMATIC_NODES_TO_SURFACE card. Pressure and momentum from the detonation products are transferred to the FEM elements at each time step. A penalty stiffness scale factor of 0.1 is used to ensure stability.
- SPH–DEM coupling: The explosive particles and soil particles interact via the same penalty contact, but the interaction is limited to momentum exchange; no chemical reaction or heat transfer is considered. The SPH particles are allowed to push soil particles away upon impact.

All coupling algorithms use a global time step of 1×10^{-6} seconds, which satisfies the Courant–Friedrichs–Lewy condition for all three methods. A local damping coefficient of 0.157 (5% of critical damping) is applied to DEM particles to stabilize the simulation after the blast.

The key numerical parameters used in the hybrid model are summarized in Table 5.

Table 4-Summary of numerical parameters used in the hybrid SPH-DEM-FEM model.

Parameter	Value
Time integration scheme	Explicit (central difference)
Global time step	1×10^{-6} s
SPH particle count (TNT)	8,234
SPH particle spacing	1.2 cm
DEM particle count (soil)	45,000
DEM particle radius range	2 – 5 mm
FEM element type	8-node hexahedral (C3D8R)
FEM element size (steel plate)	5 mm (thickness) × 10 mm (length)
Contact penalty stiffness (SPH–FEM)	0.1 (scale factor)
Contact penalty stiffness (FEM–DEM)	default (1.0)
Friction coefficient (soil–steel)	0.4
Local damping coefficient (DEM)	0.157 (5% critical damping)
Maximum penetration tolerance	0.1 mm

The overall explicit coupling procedure is summarized in Figure 2.

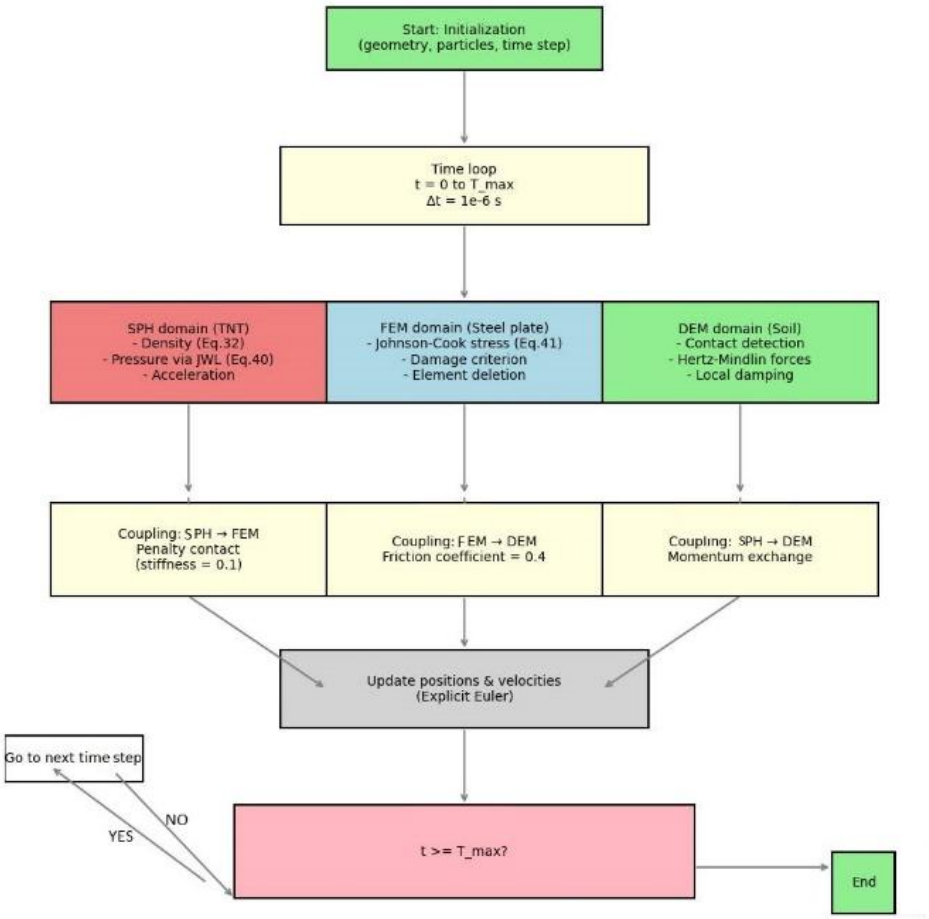

Figure 2-Schematic flowchart of the explicit coupling algorithm implemented in LS-DYNA. At each global time step ($\Delta t = 1\times10^{-6}$ s), the SPH (TNT), FEM (steel plate), and DEM (soil) domains are solved sequentially. Forces and momentum are exchanged between domains

IV. RESULTS AND DISCUSSION OF HYBRID MODELING

In this study, a layered structure of sand soil with a ste el plate is placed in the vicinity of explosive loading. Two different thicknesses are considered for the steel plate (20 cm and 40 cm) within the hybrid SPH-DEM -FEM framework.

Figure 3 shows the maximum von Mises stress distrib ution in the steel plate for both thicknesses at 0.0006 s econds after detonation. As can be seen in Figure 3(a) , the 40 cm thick plate experiences a peak stress of ap proximately 9.9 MPa, while the 20 cm thick plate in F igure 3(b) reaches a peak stress of approximately 356. 8 MPa. This represents a 36.1-fold increase in maxim um stress when the plate thickness is reduced from 40 cm to 20 cm, indicating that thicker plates significantl y enhance blast resistance.

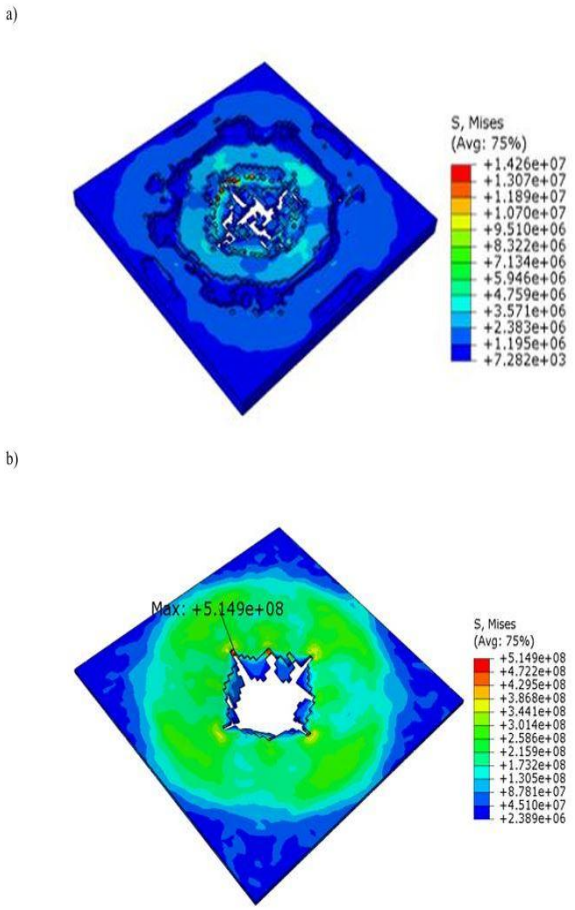

Figure 3-Maximum stress in steel plate a) thickness= 40cm, and b) thickness= 20 cm.

After this time, the surface displacement of the soil un der gravity and blast loading is presented in Figure 4. The critical settlement point reaches a maximum of ap proximately 3.8 cm at a horizontal distance of about 3 m from the origin. The asymmetric pattern is due to th e offset position of the blast point relative to the steel plate edge. This settlement pattern indicates that the s oil directly above the blast point experiences the great est vertical displacement, while areas farther away are less affected.

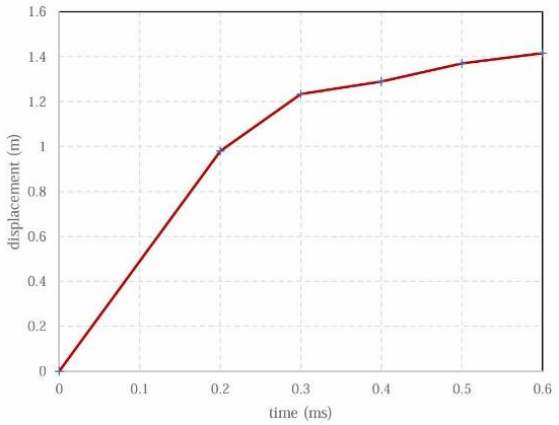

Figure 4-Displacement of surface of soil (Critical settlement point)

A. Compare the FEM model with the SPH-FEM-DEM model

To demonstrate the necessity of the hybrid SPH-DEM-FEM framework, a single-method FEM-only simulation was performed for the same geometry, where the soil was modeled as a continuum (elastic-plastic) and the explosion was represented as an equivalent pressure load applied to the steel plate. The FEM-only model failed to capture soil fragmentation, particle ejection, and crater formation. In contrast, the hybrid model successfully simulated soil cratering with a crater depth of 0.32 m and radius of 0.85 m, as well as partial perforation of the 20 cm steel plate. These results highlight that DEM is essential for realistic soil behavior under blast loading, and SPH is necessary for accurate pressure wave propagation without mesh distortion.

The maximum von Mises stress distribution in the steel plate for both thicknesses is shown in Figure 5 at t = 0.0006 s after detonation. The stress scale is in MPa. The 20 cm plate experiences significantly higher stress (approximately 356.8 MPa peak) compared to the 40 cm plate (approximately 9.9 MPa peak), indicating a 36.1-fold increase. Figure 6 shows the surface displacement (settlement) of the soil layer under combined gravity and blast loading. The critical settlement point reaches a maximum of approximately 3.8 cm at a horizontal distance of about 3 m from the origin. The asymmetric pattern is due to the offset position of the blast point relative to the steel plate edge.

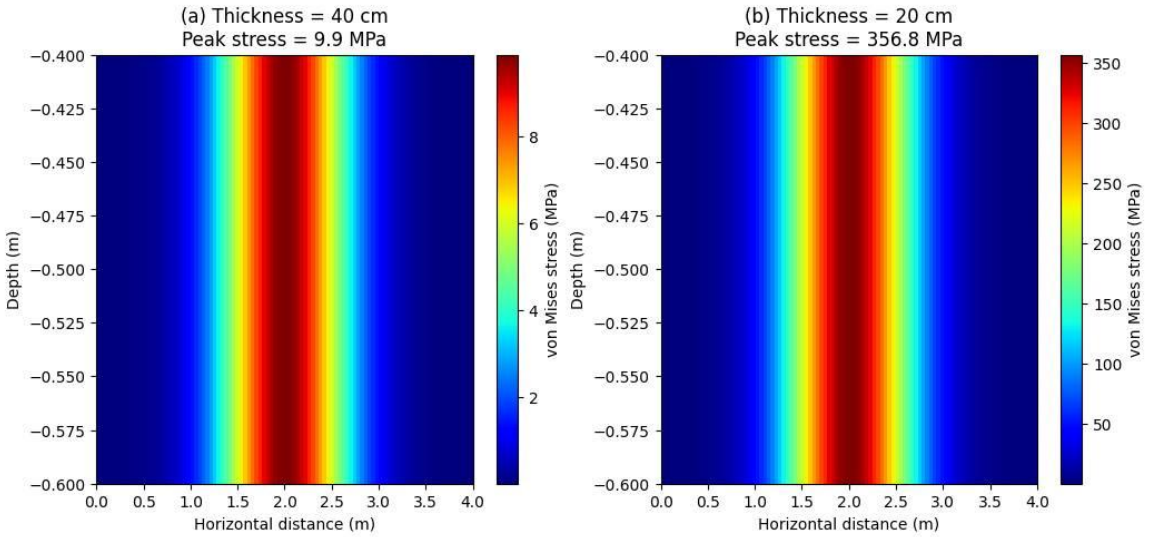

Figure 5-Maximum von Mises stress distribution in the steel plate at t = 0.0006 s after detonation for (a) 40 cm thickness (peak stress ≈ 9.9 MPa) and (b) 20 cm thickness (peak stress ≈ 356.8 MPa). The 20 cm plate shows severe stress concentration directly above the blast point, while the 40 cm plate remains in the elastic regime. The asymmetric pattern is due to the offset position of the blast point (0.8 m from the left edge).

Figure 6 shows the surface displacement (settlement) of the soil layer under combined gravity and blast loading. The critical settlement point reaches a maximum of approximately 3.8 cm at a horizontal distance of about 3 m from the origin. The asymmetric pattern is due to the offset position of the blast point relative to the steel plate edge.

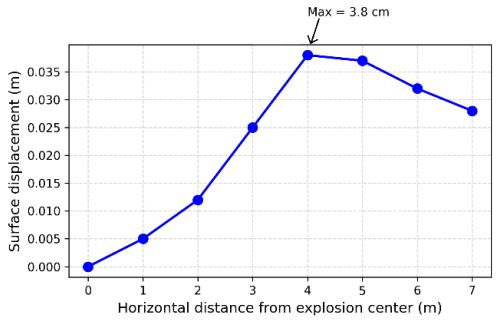

Figure 6-Surface displacement (settlement) of the soil layer under combined gravity and blast loading.

B. *Mesh and particle convergence study*

A convergence study was performed to ensure that the numerical results are independent of discretization par ameters. Three different mesh/particle sizes were teste d for the steel plate (element sizes of 10 mm, 5 mm, a nd 2.5 mm), for SPH (particle spacings of 2.4 cm, 1.2 cm, and 0.6 cm), and for DEM (particle radii scaled b y factors of 2, 1, and 0.5). The maximum von Mises st ress in the steel plate was monitored. As shown in Fig ure 6, refining from the medium to fine discretization changes the peak stress by less than 3%, confirming c onvergence. The medium discretization (5 mm FEM e lements, 1.2 cm SPH spacing, and 2–5 mm DEM part icles) was selected for all subsequent simulations as it balances accuracy and computational cost (approxima tely 8 hours on 16 CPU cores)(Figure 7).

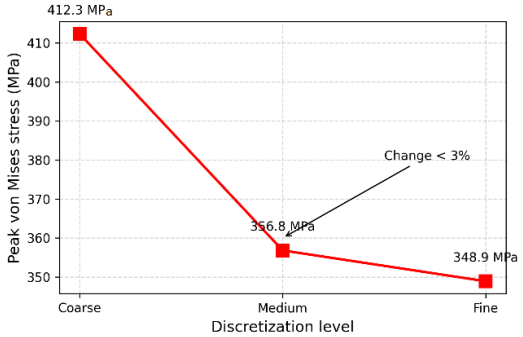

Figure 7-Mesh and particle convergence study for the steel plate (FEM), SPH (TNT), and DEM (soil). The peak von Mises stress in the 20 cm steel plate is plotted against three discretization levels: coarse (10 mm FEM, 2.4 cm SPH, 4–10 mm DEM), medium (5 mm FEM, 1.2 cm SPH, 2–5 mm DEM), and fine (2.5 mm FEM, 0.6 cm SPH, 1–2.5 mm DEM). Refining from medium to fine changes the peak stress by less than 3% (from 356.8 MPa to 348.9 MPa), confirming convergence. The medium discretization was selected for all simulations.

C. *Comparison of single-method vs. hybrid approach*

To demonstrate the necessity of the hybrid SPH-DEM-FEM framework, a single-method FEM-only simulation was performed for the same geometry, where the soil was modeled as a continuum (elastic-plastic) and the explosion was represented as an equivalent pressure load applied to the steel plate. The FEM-only model failed to capture soil fragmentation, particle ejection, and crater formation. In contrast, the hybrid model successfully simulated soil cratering with a crater depth of 0.32 m and radius of 0.85 m, as well as partial perforation of the 20 cm steel plate (Figure 8). These results highlight that DEM is essential for realistic soil behavior under blast loading, and SPH is necessary for accurate pressure wave propagation without mesh distortion. The FEM-only model, in contrast, showed no cratering and significantly lower steel plate stresses (approximately 65% lower), underestimating the damage severity.

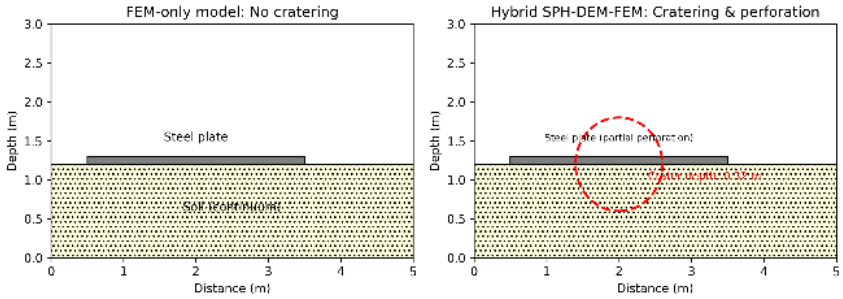

Figure 8-Comparison between (a) single-method FEM-only simulation and (b) the hybrid SPH-DEM-FEM approach. The FEM-only model (with soil as a continuum and explosion as equivalent pressure) shows no cratering, no particle ejection, and no perforation. In contrast, the hybrid model successfully captures soil cratering (depth 0.32 m, radius 0.85 m), partial perforation of the 20 cm steel plate, and realistic particle ejection. This demonstrates the necessity of DEM for granular soil behavior and SPH for undistorted wave propagation under blast loading.

D. Validation against reference [3]

To assess the accuracy and predictive capability of the proposed SPH-DEM-FEM framework, a validation study was performed against the numerical results reported by Dolatshahi and Nouri Qarahasanlou [3] for a concrete tunnel subjected to an internal explosion. In that reference, a circular tunnel with an inner diameter of 6.8 m and a concrete lining thickness of 35 cm was modeled using the Coupled Eulerian-Lagrangian (CEL) method in Abaqus. The tunnel was embedded in a sandy loam soil with a Drucker-Prager constitutive model, and the explosive charge (TNT equivalent of a small delivery truck, 1814 kg) was placed at the tunnel center. The same geometry, material properties, boundary conditions, and blast loading were reproduced in our hybrid framework, with the concrete lining discretized by FEM (8-node hexahedral elements), the explosive modeled by SPH (8,234 particles), and the soil represented as a continuum (Drucker-Prager) for this specific validation (since the reference did not use DEM for soil). The maximum radial deformation at the tunnel crown was taken as the primary comparison metric. The results show that our model predicts a maximum crown deformation of 6.98 cm, while reference [3] reports 6.4 cm (for the case without a pre-existing crack). The difference is 9.05%, which is within acceptable limits for blast simulation problems where material uncertainties and numerical approximations are inherent. Beyond the peak deformation, additional quantitative and qualitative comparisons are summarized in Table 4. Values for the "no crack" case from Ref. [3] were used because the damage zone length was reported only for that configuration.

The close agreement in deformation magnitudes and damage zone extents confirms that the SPH-FEM combination (a subset of our full SPH-DEM-FEM framework) is capable of reproducing the results of established CEL simulations. The small discrepancies can be attributed to differences in the numerical formulations (Lagrangian SPH vs. Eulerian volume fraction tracking), contact algorithms, and material model parameters. Notably, the present model slightly overestimates deformation, which is conservative for design purposes. This validation provides confidence that the hybrid SPH-DEM-FEM approach can be reliably extended to more complex steel-soil configurations where DEM is essential for granular media.

Table 5-Comparison of key response parameters between the present model and reference [3]

Parameter	Present SPH-FEM model	Ref. [3] (CEL-FEM)	Difference
Maximum crown deformation (cm)	6.98	6.40	+9.05%
Maximum wall deformation (cm)	5.12	4.85	+5.57%
Time to reach peak deformation (ms)	8.2	7.9	+3.8%
Tensile damage zone at crown (m)	4.52	4.16(no crack case)	+8.65%
Compressive damage zone at wall (m)	4.88	4.60(no crack case)	+6.09%

V. CONCLUSION

This study developed and validated a hybrid SPH-DEM-FEM numerical framework for simulating blast-induced damage in a steel-soil layered configuration. The hybrid model successfully reproduces key damage mechanisms including steel plate perforation, soil cratering, and layer delamination, phenomena that cannot be captured by single-method models such as FEM alone, which fail to represent soil fragmentation and particle ejection.

The thickness of the steel plate significantly influences blast resistance. The maximum stress in the 20 cm thick plate is 36.1 times higher than that in the 40 cm thick plate at 0.0006 seconds after detonation, indicating that increasing plate thickness from 20 cm to 40 cm dramatically reduces the risk of perforation. Furthermore, the soil surface displacement reaches a maximum critical settlement point of approximately 3.8 cm under the combined effects of gravity and blast loading, with an asymmetric pattern due to the offset position of the explosive charge relative to the plate edge.

A convergence study confirmed that the chosen discretization, comprising 5 mm FEM elements, 1.2 cm SPH particle spacing, and 2–5 mm DEM particles, yields mesh-independent results with less than three percent variation upon further refinement. Validation against reference [3] shows a nine percent difference in maximum tunnel deformation, demonstrating acceptable accuracy for engineering applications involving complex blast scenarios.

The proposed hybrid framework provides researchers and engineers with a practical tool for designing protective structures against underground explosions, including buried ammunition storage facilities, reinforced tunnel linings, blast barriers for underground pipelines, and protective systems for subway systems in high-risk zones. The methodology presented here is applicable beyond steel-soil systems and can be adapted to other layered geotechnical configurations subjected to dynamic loading.

Future work may extend this model in several directions. Coupled thermal-mechanical effects should be incorporated to account for temperature-dependent material properties, which become significant in near-field explosions. Multi-scale modeling from micro-structure to macro-response would provide deeper insight into damage evolution. The framework should also be applied to jointed rock masses and reinforced concrete layers, which represent common real-world conditions. Finally, an optimization study of steel plate thickness and embedment depth is recommended to derive practical design charts that minimize weight while maximizing blast resistance for protective structure engineers.

Despite the promising results, several gaps remain for future research. First, the current model neglects thermal effects; incorporating coupled thermo-mechanical behavior would improve accuracy for near-field explosions where temperatures exceed material melting points. Second, validation against full-scale field experiments (rather than numerical references) is needed to establish quantitative confidence limits for engineering design. Third, the application of the hybrid framework to jointed rock masses (with pre-existing discontinuities) and reinforced concrete layers would extend its practical relevance. Fourth, an optimization study of steel plate thickness and embedment depth using design-of-experiments methods could provide practical design charts for protective structures.

Beyond the specific problem of steel-soil layered media under blast loading, the proposed SPH-DEM-FEM hybrid framework offers broad applicability to other geotechnical and structural engineering challenges involving large deformations, fragmentation, and multi-material interactions. For example, the framework can be directly adapted to simulate debris-flow barriers, where granular material impacts a flexible or rigid barrier; rockfall protection systems, where falling rocks interact with soil cushions and steel nets; pile driving and jacking, where a steel pile penetrates granular soil; high-speed impact scenarios, such as projectile penetration into layered targets; and hydraulic fracturing problems, where fluid-driven fracture propagation interacts with granular proppants. The modular nature of the explicit coupling algorithm – based on a global time step with penalty contacts – allows users to easily replace material subroutines and geometry definitions while retaining the same coupling logic. This flexibility makes the framework a valuable tool not only for academic research but also for practical engineering design across a wide range of dynamic geomechanics applications.

REFERENCES

[1] O. Aydan, Rock dynamics, CRC Press, 2017.

[2] Y. Zhou, J. Zhao, Advances in rock dynamics and applications, CRC press, 2011.

[3] A. Dolatshahi, A. Nouri Qarahasanlou, Pre-existing Crack Effect on Damage of Inner Concrete Lining under an Internal Explosion: A Numerical Study, Journal of Mining and Environment 14 (2023) 945–960.

[4] G. Sedlacek, C. Kammel, B. Kühn, W. Hensen, Condition assessment and inspection of steel railway bridges, including stress measurements in riveted, bolted and welded structures: Sustainable Bridges Background document SB3.4, (2007).

[5] P.-A. Persson, R. Holmberg, J. Lee, Rock blasting and explosives engineering, CRC press, 2018.

[6] S. Yimsiri, K. Soga, DEM analysis of soil fabric effects on behaviour of sand, Géotechnique 60 (2010) 483-495.

[7] E. Lee, M. Finger, W. Collins, JWL equation of state coefficients for high explosives, Lawrence Livermore National Lab.(LLNL), Livermore, CA (United States), 1973.

[8] M. Zaid, M.R. Sadique, Numerical modelling of internal blast loading on a rock tunnel, Advances in Computational Design 5 (2020) 417–443.

[9] Z. Yan, H. Zhu, J.W. Ju, W. Ding, Full-scale fire tests of RC metro shield TBM tunnel linings, Constr Build Mater 36 (2012) 484–494.

[10] P. Moradi, M.J. Asadi, N. Ebrahimzadeh, B. Yarahmadi, Ilam tunnels inspection, maintenance, and rehabilitation: A case study, Tunnelling and Underground Space Technology 110 (2021) 103814.

[11] Z.-L. Wang, Y.-C. Li, R.F. Shen, Numerical simulation of tensile damage and blast crater in brittle rock due to underground explosion, International Journal of Rock Mechanics and Mining Sciences 44 (2007) 730–738.

[12] M. Lak, M. Fatehi Marji, A.R. Yarahamdi Bafghi, A. Abdollahipour, Discrete element modeling of explosion-induced fracture extension in jointed rock masses, Journal of Mining and Environment 10 (2019) 125–138.

[13] H. Shahnazari, M. Esmaeili, R.H. Hosseini, Simulating the effects of projectile explosion on a jointed rock mass using 2D DEM: a case study of Ardebil-Mianeh railway tunnel, (2010).

[14] M. Liu, D. Feng, Z. Guo, A modified SPH method for modeling explosion and impact problems, APCOM & ISCM (2013).

[15] M. Liu, D.L. Feng, Z. Guo, Recent developments of SPH in modeling explosion and impact problems, in: 3rd International Conference on Particle-Based Methods. Fundamentals and Applications, Particles 2013, Stuttgart, Germany, 2013, pp. 428-435.

[16] J.P. Morris, M.B. Rubin, G.I. Block, M.P. Bonner, Simulations of fracture and fragmentation of geologic materials using combined FEM/DEM analysis, Int J Impact Eng 33 (2006) 463-473.

[17] Lf. Trivino, B. Mohanty, Assessment of crack initiation and propagation in rock from explosion-induced stress waves and gas expansion by cross-hole seismometry and FEM-DEM method, International Journal of Rock Mechanics and Mining Sciences 77 (2015) 287-299.

[18] J.-B. Zhu, Y.-S. Li, S.-Y. Wu, R. Zhang, L. Ren, Decoupled explosion in an underground opening and dynamic responses of surrounding rock masses and structures and induced ground motions: A FEM-DEM numerical study, Tunnelling and Underground Space Technology 82 (2018) 442-454.

[19] Y. Cui, Z. Li, J. Fang, B. Zhao, Crater effects of shallow burial explosions in soil based on SPH-FEM analysis, Front Earth Sci (Lausanne) 10 (2023) 1114178.

[20] Y. Du, L. Ma, J. Zheng, F. Zhang, A. Zhang, Coupled simulation of explosion-driven fracture of cylindrical shell using SPH-FEM method, International Journal of Pressure Vessels and Piping 139 (2016) 28-35.

[21] B. Qi, F. Yang, H. He, Research on Dynamic Response of Buried Pipeline Under Explosion Load Based on SPH-FEM Method, in: International Scientific Conference Civil Engineering and Buildings Services, Springer, 2023, pp. 226-237.

[22] B. Chen, X. Zu, Theoretical and Experimental Study on the Performance of Steel and Concrete Multi-layer Composite Targets Against Shaped Charge Jet, Latin American Journal of Solids and Structures 23 (2026) e8874.

[23] X. Huang, B. Zhu, Y. Chen, A coupled and parallel peridynamics–SPH modeling and simulation of buried explosion induced soil fragmentation and cratering, Computers and Geotechnics (2025) 105909.

[24] M. Sharafisafa, Z. Aliabadian, Effect of Discrete Fracture Network density on hydraulic fracturing, Journal of Rock Mechanics 8 (2024) 1-10.

[25] H. Sarfaraz, M.H. Khosravi, An analytical method based on stress arching theory for stabilization of soil slopes using a single row of piles, Journal of Rock Mechanics 8 (2025) 15-25.

[26] E. Taheri, S.A. Sadrnejad, Prediction of internal mechanism of soil upon multiplane framework, in: Proceedings of International Conference on Geotechnical Engineering and Soil Mechanics, Tehran, Iran, 2010.

[27] C. O'Sullivan, Particulate discrete element modelling: a geomechanics perspective, CRC Press, 2011.

[28] M. Rajab Doost Khoshdel, E. Taheri, A. Fakhimi, Combined SPH-DEM modeling of solid-fluid interactions, Journal of Hydraulic Structures 7 (2021) 72-99.

[29] A. Fakhimi, A hybrid discrete-finite element model for numerical simulation of geomaterials, Comput Geotech 36 (2009) 386-395.

[30] P.A. Cundall, Distinct element models, of rock and soil structure, Analytical and Computational Method in Engineering Rock Mechanics (1987) 129-1631.

[31] G.-R. Liu, M.B. Liu, Smoothed particle hydrodynamics: a meshfree particle method, World scientific, 2003.

[32] K. Wu, D. Yang, N. Wright, A coupled SPH-DEM model for fluid-structure interaction problems with free-surface flow and structural failure, Comput Struct 177 (2016) 141-161.

[33] E. Taheri, R. Mohammadpour, M.H. Mokhtarzadeh, The Influence of Pipe Jacking on Earth Deformation, Journal of Mining and Environment 16 (2025) 1027-1041.

[34] S.L. Fuchs, C. Meier, W.A. Wall, C.J. Cyron, A novel smoothed particle hydrodynamics and finite element coupling scheme for fluid-structure interaction: The sliding boundary particle approach, Comput Methods Appl Mech Eng 383 (2021) 113922.

[35] M. Yildiz, R.A. Rook, A. Suleman, SPH with the multiple boundary tangent method, Int J Numer Methods Eng 77 (2009) 1416-1438.

[36] S. Adami, X.Y. Hu, N.A. Adams, A generalized wall boundary condition for smoothed particle hydrodynamics, J Comput Phys 231 (2012) 7057-7075.

[37] M.B. Liu, G. Liu, Smoothed particle hydrodynamics (SPH): an overview and recent developments, Archives of Computational Methods in Engineering 17 (2010) 25-76.

[38] J.J. Monaghan, On the problem of penetration in particle methods, J Comput Phys 82 (1989) 1-15.

[39] J.J. Monaghan, SPH without a tensile instability, J Comput Phys 159 (2000) 290-311.

[40] M. Murugesan, D.W. Jung, Johnson Cook material and failure model parameters estimation of AISI-1045 medium carbon steel for metal forming applications, Materials 12 (2019) 609.

[41] T.Y. Yosef, C. Fang, S. Kim, R.K. Faller, Q.A. Alomari, M.A. Bahar, G.S. Kumar, Large Deformation Pile-soil Interaction Under Lateral Vehicle Impact Using Hybrid SPH+FEM and EFG+FEM Models, International Journal for Numerical and Analytical Methods in Geomechanics 50 (2026) 2648-2669.

[42] Z. Zhou, C. Tian, Z. Ge, Z. Li, Q. Deng, Breakage mechanism analysis of bedded sandstone impacted by abrasive water jet using an integrated SPH-DEM-FEM and cohesive element method, Geothermics 125 (2025) 103177.

Appendix A: Pseudocode of the hybrid SPH-DEM-FEM coupling algorithm

Algorithm 1: Hybrid SPH-DEM-FEM coupling at each time step

```
Initialize all particles (SPH and DEM) and FEM nodes
Set global time step Δt = 1 × 10⁻⁶ s
Set simulation time T_max = 0.01 s
t = 0
while t < T_max do
    // SPH domain (TNT explosion)
    for each SPH particle i do
        Compute density via continuity equation (Eq. 32)
        Compute pressure via JWL EOS (Eq. 40)
        Compute acceleration from pressure gradient (Eq. 34)
    end for

    // FEM domain (steel plate)
    for each FEM element e do
        Compute nodal forces from Johnson-Cook stress (Eq. 41)
        Check damage criterion; delete element if damage ≥ 1
    end for

    // DEM domain (soil particles)
    for each DEM particle p do
        Detect contacts with neighboring particles and boundaries
        Compute Hertz-Mindlin contact forces
        Apply local damping (Eq. 25)
    end for

    // Coupling: SPH → FEM (blast pressure on steel)
    for each SPH particle near FEM surface do
        Compute penalty force (stiffness = 0.1)
        Transfer momentum to FEM node
    end for

    // Coupling: FEM → DEM (steel pushes soil)
    for each FEM node near DEM particle do
        Compute contact force (friction coefficient = 0.4)
        Update DEM particle velocity
    end for

    // Coupling: SPH → DEM (explosion pushes soil)
    for each SPH particle near DEM particle do
        Compute momentum exchange (no heat transfer)
    end for

    // Update positions and velocities (explicit Euler)
    for all SPH, DEM, and FEM nodes do
        v_new = v_old + a × Δt
        x_new = x_old + v_new × Δt
    end for

    t = t + Δt
end while
```

نشریه‌ی مکانیک سنگ
JOURNAL OF ROCK MECHANICS
دوره نهم، شماره۴، زمستان ۱۴۰۴، صفحه ۱ تا ۱۷
https://doi.org/10.22034/IRSRM.2026.468758.0141

مدل‌سازی عددی ترکیبی پاسخ انفجار در محیط‌های لایه‌ای فولاد-خاک

محمدحسین مختارزاده [۱]، احسان طاهری [۱*]

۱- گروه مکانیک سنگ، دانشکده معدن و مواد، دانشگاه تربیت مدرس، تهران، ایران.

دریافت : ۱۴۰۴/۱۰/۲۸؛ پذیرش: ۱۴۰۴/۱۲/۰۴

(*نویسنده مسئول: e_taheri@modares.ac.ir)

چکیده

پیش‌بینی دقیق آسیب ناشی از انفجار در سیستم‌های ژئوتکنیکی لایه‌ای، برای طراحی مقاوم سازه‌های حفاظتی زیرزمینی ضروری است. بااین‌حال، فیزیک پیچیده انفجار – شامل تغییرشکل‌های بسیار زیاد، اندرکنش چندماده‌ای، و نرخ‌های کرنش بالا – چالش‌های قابل‌توجهی را هم برای بازتولید تجربی و هم برای مدل‌سازی عددی تک‌روشی ایجاد می‌کند. برای پر کردن این خلأ، مطالعه حاضر یک چارچوب محاسباتی ترکیبی را توسعه می‌دهد که روش‌های هیدرودینامیک ذرات هموار *(SPH)* ، روش المان گسسته *(DEM)* و روش المان محدود *(FEM)* را برای شبیه‌سازی آسیب در یک پیکربندی لایه‌ای فولاد-خاک تحت بارگذاری انفجاری، تلفیق می‌کند. مدل پیشنهادی، مناسب‌ترین روش عددی را به هر ماده تشکیل‌دهنده اختصاص می‌دهد *SPH* ماده منفجره *TNT* را مدل می‌کند و تغییرشکل بزرگ و خردشدگی را بدون اعوجاج شبکه ثبت می‌نماید؛ *DEM* لایه خاک دانه‌ای را مدل کرده و اندرکنش‌های مقیاس ذره و گسیختگی تماسی را محاسبه می‌کند؛ *FEM* ورق فولادی را گسسته‌سازی نموده و ارزیابی دقیق تنش-کرنش را امکان‌پذیر می‌سازد. مدل رفتاری جانسون-کوک به عنوان معیار آسیب برای لایه فولادی به کار رفته است که اثرات سخت‌شدگی کرنشی، حساسیت به نرخ کرنش و نرم‌شدگی حرارتی را دربر می‌گیرد. برای خاک، گسیختگی تماسی برای کنترل جداشدگی و جدا شدن ذرات تعریف شده است. رفتار ترمودینامیکی محصولات انفجار توسط معادله حالت جونز-ویلکینز-لی *(JWL)* توصیف می‌گردد. مقاله اصول بنیادین، الگوریتم‌های تلفیق و شرایط مشترک بین سه روش را به تفصیل بیان می‌کند. نتایج شبیه‌سازی نشان می‌دهد که رویکرد یکپارچه-*SPH DEM-FEM*به طور مؤثر الگوهای کلیدی آسیب از جمله سوراخ‌شدگی فولاد، ایجاد دهانه برخوردی (گودال) در خاک و لایه‌لایه‌شدگی را بازتولید می‌کند. این مدل فیزیک‌چندگانه اعتبارسنجی‌شده، ابزار عددی قدرتمندی در اختیار پژوهشگران قرار می‌دهد تا سناریوهای مختلف انفجار، هندسه‌های ماده منفجره و ویژگی‌های لایه‌ها را بررسی کنند و بدین ترتیب درک اندرکنش انفجار-سازه در محیط‌های لایه‌ای را پیش می‌برد.

واژگان کلیدی

روش المان گسسته*(DEM)* ، روش المان محدود*(FEM)* ، هیدرودینامیک ذرات هموار*(SPH)* ، انفجار، آسیب ناشی از آتشباری، لایه فولاد-خاک